Engineering with Computers
https://doi.org/10.1007/s00366-025-02216-x

ORIGINAL ARTICLE

A hybrid Lattice-Boltzmann model for hydro-electrochemical modeling and sensitivity analysis of crystallization potential in nanoporous media. Part I: simulation model

Fedor Bukreev[1,2] · Adrian Kummerländer[1,3] · Julius Jeßberger[1,3] · Dennis Teutscher[1,2] · Shota Ito[1,2] · Stephan Simonis[1,3] · Davide Dapelo[4] · Mohaddeseh M. Nezhad[4] · Hermann Nirschl[1,2] · Mathias J. Krause[1,2,3]

Received: 24 February 2025 / Accepted: 21 September 2025

Abstract
This is the first in a two paper series investigating the process of hydro-electrochemical crystallization in nano-scale porous media at the supersaturation stage. In Part I, the synchronous numerical model for integrated hydro-electro-chemo-dynamics simulation, and sensitivity analysis of nano-scale crystallization potential, is developed within the Lattice-Boltzmann framework using the open-source software library OpenLB. The present work makes use of a reactive Navier-Stokes-Poisson-Nernst-Planck (RNSPNPE) Equation system for three types of ions in the moving carrier fluid and in the presence of a dynamic electric field. We propose a time-adaptive splitting approach to decouple the system, using Lattice-Boltzmann method (LBM) for the discretization of the equations. We apply an algorithmic differentiation approach for calculation of the parameters' sensitivities. The complete solver is validated with analytical solutions, on the basis of a first-order convergence criterion. The sensitivity approach is validated by comparison to predictions achieved from a sensitivity analysis performed with finite difference method, enabling a meaningful analysis of crystallization potential on the nanopore level. The work integrates the RNSPNPE system into a framework specifically designed for the supersaturation process investigations of the crystallizing species within nanoporous geometries. This work proposes a model that couples fluid flow, electric potential, and ion transport in a reactive setting. A novel aspect of this work lies in the seamless integration of sensitivity analysis algorithms into the Lattice-Boltzmann physicochemical solver, extending the LBM beyond its conventional role as a fluid-flow solver and employing it as a tool for sensitivity analysis. This solver can be applied to other nanoscopic and microscopic chemical electro-hydrodynamics processes as well.

Keywords Nanoporous geometry · Phosphates crystallization · Saturation · Nano-scale · Electro-hydrodynamics · Lattice-Boltzmann method · Automatic differentiation

1 Introduction

The investigation of chemical processes and surface reactions can be conducted across various scales, ranging from the nanoscopic to the microscopic. These scales define the size of the control volume where the reaction is analyzed. In heterogeneous porous systems, reactions occur at multiple scales depending on the pore size distribution. Extensive research has been conducted at both the macroscopic scale, where the entire reactor volume is considered, and the microscopic scale, focusing on individual pore structures. However, this study primarily focuses on the nanoscale, where reactions occur at the finest level of pore confinement.

✉ Fedor Bukreev
fedor.bukreev@kit.edu

[1] Lattice Boltzmann Research Group (LBRG), Karlsruhe Institute of Technology (KIT), Straße am Forum 8, Karlsruhe 76131, Germany

[2] Institute of Mechanical Process Engineering and Mechanics (MVM), Karlsruhe Institute of Technology (KIT), Straße am Forum 8, Karlsruhe 76131, Germany

[3] Institute for Applied and Numerical Mathematics (IANM), Karlsruhe Institute of Technology (KIT), Englerstraße 2, Karlsruhe 76131, Germany

[4] Department of Civil and Environmental Engineering, School of Engineering, University of Liverpool, Brownlow Hill, Liverpool L69 3GH, UK

Published online: 11 October 2025

In the present work, we focus on the numerical approach in the nanoscopic scale, and the relevant lengths are comprised between around 40 nanometers (most frequent pore diameters of the calcium silicate hydrate (CSH) micro-particles CIRCOSIL). An experimentally fitted reaction kinetics equation is often sufficient for simulation of large industrial reactors and has the advantage of covering large scales with minimal computational effort [1]. Unfortunately, in most cases such macroscopic full reactor simulations can not lead to a complete understanding of the detailed processes, when the interaction between chemical species is firmly prescribed by an empirically constructed polynomial [2]. To recover small-scale process information, finer measures must be taken, which require more expensive experiments and apparatus or more complex computational techniques.

A suitable example to represent the different abstraction levels is phosphate adsorption from waste water using porous micro-CSH particles as adsorbent. Investigating this process on the macroscopic scale allows one to find the overall mass of adsorbed phosphate assuming standard linear, Langmuir, or Freundlich sorption isotherms together with multiple diffusion mechanisms, namely film and pore diffusion (see for example [3] and references therein). As mentioned above, simulations of this type are based on experimentally fitted adsorption data and do not provide insight on the separate process steps and the respective dynamics. In contrast to that, modeling on the pore-scale level where the actual reaction occurs promises to provide a deeper understanding of the process details like electrically driven movement of dissolved ions in the pores, desorption of bounding metal ions, and their reaction with adsorbate ions. In the present work, the adsorption in the pore-scale is considered as nanoscopic. Thus, chemical adsorption is mainly characterized by a crystallization reaction on the pore surface. The numerical simulation of this phenomenon is typically based on a crystallization model, a system of equations describing the species dynamics in the surrounding liquid, and its numerical discretization. Adsorption as an example of a standard pore-scale chemical process, where crystallization also belongs to, can be divided into the following general steps:

1. migration of reacting ions from bulk to the pore entrance (diffusive, hydraulic and electric transport)
2. migration of ions through pore volume (diffusive, hydraulic and electric transport)
3. contact of ions with pore wall leading to dissolution of calcium cations
4. saturation of reactants at the soil surface
5. distinct nucleation of the adsorbate ion based crystal at the point with most appropriate conditions (saturation product above one and low surface tension)
6. layer-wise growth of the crystal.

On example of the phosphate crystallization in the CSH pores, these steps are schematically presented in Fig. 1.

The present work considers the first four steps without pore volume change due to dissolution and crystallization processes, assuming very small timescales regarded here. To do so, the chemical species are modeled as ions that are influenced by fluid motion and an electric field. Previously, Kler et al. [4] have investigated the electrodynamic system on a microfluidic chip with the finite elements method (FEM), using a free-slip boundary condition for the carrier fluid motion. Barnett et al. [5] discretized the pore-scale electrochemical ionic flow, described by the Stokes-Poisson-Nernst-Planck equation system, using the finite volume method. Fuel cells with multiphase (water/air) flow and dissolved ions have been modeled with the LBM by Ryan et al. [6]. An LBM discretization of a full set of formulations describing an electro-reactive system with chemical-reaction-driven phase change has been presented by Zhang and Wang [7] and used to model for precipitation and dissolution cases. Notably, the use of LBM has become popular in battery modeling [8, 9]. The electro-kinetic system discretized with LBM was analytically also validated by Tian et al. [10]. The principles of electric double layer (EDL) theory relevant to surface reactions at the nano- and micro-levels can be found in [11]. Nevertheless, these surface reactions have

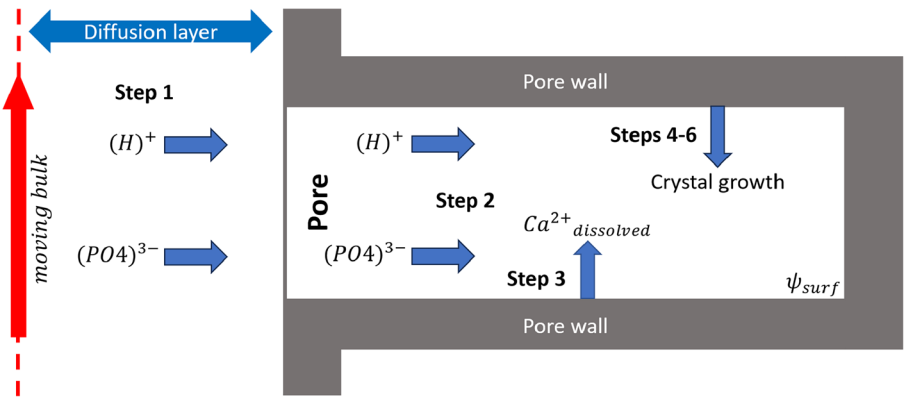

Fig. 1 General pore-scale multiphase fluid-solid chemical process with chemical species considered as solved ions in a carrier fluid

not yet been investigated numerically on the pore level considering the full system complexity, i.e. hydro-, electro- and chemo-dynamics. This work intends to fill this research gap by presenting an integrated model within the LBM framework. As LBM is well-suited for modeling nano- and micro-level multiphysics problems [12–15] due to its capability to efficiently simulate such systems, leveraging its parallelizability and the simplicity of its algorithm [16, 17].

In the current work, in its first part, the integrated dynamic hydro-electrochemical model with LBM discretization and automatic sensitivity assessment for a nanoscale porous geometry is proposed. Model equations are presented in Sect. 2. The model is discretized with LBM and coupled to the automatic differentiation (AD) algorithm in the C++ based open-source software library *OpenLB* [18, 19] (https://www.openlb.net, Sect. 3). In Sect. 4 the system components are validated step-wise on analytical solutions. Starting with the Poisson equation solver validation, going through the Poisson-Nernst-Planck system, and ending with the electro-osmosis analytical example computed using the Navier–Stokes-Poisson-Nernst-Planck equation system. Section 5 presents the validation of the AD sensitivity calculation approach against a set of results achieved from the finite differences method (FDM). To the best of the authors' knowledge, there is no tool for automatic sensitivity analysis of supersaturating reaction systems on the pore level. In the second part of the research, the solver is applied for sensitivity analysis of simplified two-dimensional nanoporous geometries representing open and blind pores. Subsequently, a realistic three-dimensional resolved nanoporous geometry is simulated, and sensitivity analysis is conducted using the integrated automatic sensitivity analysis algorithms. Finally, conclusions about the influence of factors such as pore width and length, surface Helmholtz potential, carrier fluid velocity, and reactants bulk concentrations are drawn with an outlook for a full crystallization simulation and derivation of a macro-model which can be used for the macro-simulation of complete phosphate crystallization reactors.

2 Methodology

2.1 Governing conservation equations

The present model is developed by first selecting a global approach, which, in this case, is the Eulerian ansatz with bidirectional coupling and a Strang splitting assumption. This assumption implies that, within a single time step, the variables from other equations remain constant while the current equation is solved. The model equations and connections between them are presented in Fig. 2. There is only one liquid phase with three solved ionic components, and no explicit interface is modeled. Each ion is indicated by i. Its concentration, C_i, is governed by diffusion—described by the diffusion coefficient D_i—and by advection, which comprises movement induced by the carrier fluid $\boldsymbol{u}_{\mathrm{fl}}$ and by the electric field $\boldsymbol{u}_{\mathrm{el},i}$. In the boundary cells, the ion concentration is updated by summing over the reaction terms $R_{k,i} = \vartheta_{k,i} r_k$, where k is the reaction index, $\vartheta_{k,i}$—stoichiometric coefficient of the species i in the reaction k and r_k—the corresponding reaction rate:

$$\partial_t C_i + \nabla \cdot \left(C_i \left(\boldsymbol{u}_{\mathrm{fl}} + \boldsymbol{u}_{\mathrm{el},i} \right) \right) = D_i \Delta C_i + \sum_k R_{k,i}. \tag{1}$$

The equation above is called reactive Nernst-Planck equation (RNPE).

The carrier fluid velocity is determined from the usual incompressible Navier–Stokes mass and momentum conservation equations forced by the electric term $\boldsymbol{F}_{\mathrm{el}}$ as well

$$\nabla \cdot \boldsymbol{u} = 0, \tag{2}$$

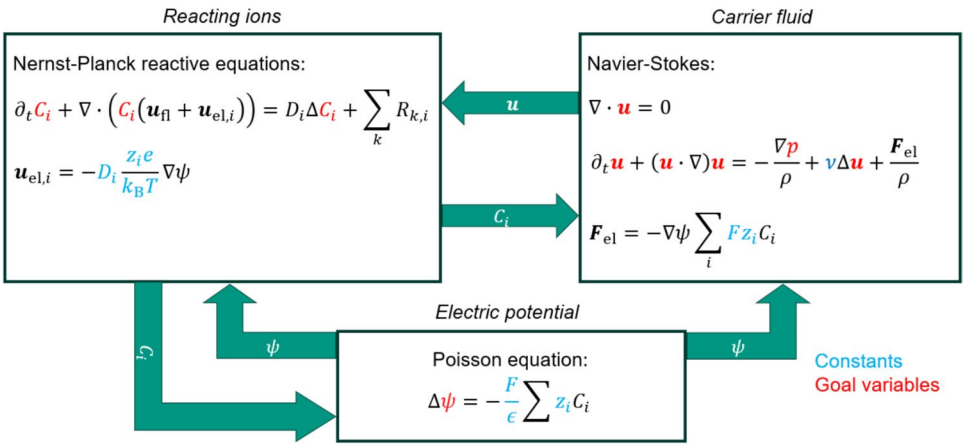

Fig. 2 Full Eulerian equation system for a hydro-electro-chemical simulation of an ionic supersaturation process and dissolution reactions in resolved nanopores

$$\partial_t \boldsymbol{u} + (\boldsymbol{u} \cdot \nabla)\boldsymbol{u} + \frac{1}{\rho}\nabla p = \nu \Delta \boldsymbol{u} + \frac{\boldsymbol{F}_{\mathrm{el}}}{\rho}. \tag{3}$$

Here, ρ, ν and p are the carrier fluid density, kinematic viscosity and pressure, respectively. The concentrations of the ions are assumed to be small enough to leave the liquid's density and viscosity unaltered.

The electric field is computed from the potential ψ, which is assumed to obey the Poisson's equation (PE)

$$\Delta \psi = -\frac{F}{\epsilon} \sum_i z_i C_i, \tag{4}$$

where F is the Faraday constant, ϵ is the total carrier fluid permittivity and z_i the ion valence. The coupling terms $\boldsymbol{u}_{\mathrm{el},i}$ and F_{el} can be determined from the electric potential as follows:

$$\boldsymbol{u}_{\mathrm{el},i} = -D_i \frac{z_i e}{k_{\mathrm{B}} T} \nabla \psi, \tag{5}$$

$$\boldsymbol{F}_{\mathrm{el}} = -(\nabla \psi) F \sum_i z_i C_i. \tag{6}$$

The e is an elementary charge, and the $k_{\mathrm{B}}T$ term is the product of the Boltzmann constant and temperature.

The total resulting system is called reactive Navier–Stokes-Poisson-Nernst-Planck equation system (RNSPNPE).

2.2 Reaction system

In the present work, two parallel processes are considered as an example application: the dissolution of calcium cations from the pore surface (7), and the saturation of phosphate, hydrogen, and calcium ions, which enables the formation of octacalcium phosphate (OCP) there (8). The reaction system can be written in ionic form as follows:

$$\mathrm{CSH} + 1.66\mathrm{H}^+ \leftrightarrows 0.86\mathrm{Ca}^{2+}, \tag{7}$$

$$8\mathrm{Ca}^{2+} + 6\mathrm{PO}_4^{3-} + 2\mathrm{H}^+ \xrightarrow{\text{saturation}} \mathrm{Ca}_8\mathrm{H}_2(\mathrm{PO}_4)_6 \downarrow. \tag{8}$$

The stoichiometric dissolution coefficients are set according to [20]. More information about OCP and its further conversion to hydroxyapatite can be found in [21].

The common form for the crystallization and dissolution reaction rates used in this work is [20, 22]

$$r = \frac{k_{\mathrm{sr}}}{\triangle x}(\Omega - 1)^n. \tag{9}$$

Here, k_{sr} is the surface specific reaction rate constant $[\mathrm{mol\,m^{-3}\,s^{-1}}]$, the saturation product $\Omega = \left(\mathrm{IAP}/K_{\mathrm{sp}}\right)^{1/\sigma_{\mathrm{T}}}$ with ionic activity product $\mathrm{IAP} = \prod_i a_i^{\vartheta_i}$ and saturation point constant K_{sp}. n is the order of crystallization; in case of dissolution, it is just one. The parameters k_{sr} and K_{sp} can be defined experimentally, by molecular dynamics simulation, or special chemical software like PHREEQC [23]. σ_{T} is the Temkin coefficient taken for the saturation product estimation. The ion activity a_i is calculated by the Debye-Hückel extended theory [24].

$$a_i = \gamma_i C_i, \tag{10}$$

$$\log \gamma_i = -A z_i^2 \frac{\sqrt{I}}{1 + B a_0 \sqrt{I}}, \tag{11}$$

$$I = \frac{1}{2} \sum_i z_i^2 C_i. \tag{12}$$

The γ_i is the ion activity coefficient, which is computed with ionic strength I, smallest distance between interacting ions a_0 and case-specific constants A and B, which can be found in sum with all other used parameters in Table 1.

3 Discretization

3.1 Lattice-Boltzmann method (LBM)

To enable an efficient computation of large resolved realistic porous domains on CPU-GPU HPC clusters, the built-up RNSPNPE system is approximated with LBM, which draws inspiration from microscopic gas kinetic theory [31]. In this framework, molecules are treated as hard spheres that undergo elastic collisions and motion. The probability density function (PDF) $f(\boldsymbol{x}, \boldsymbol{\xi}, t)$ is defined as the probability of finding a particle within the elementary element $[\boldsymbol{x}, \boldsymbol{x} + d\boldsymbol{x}] \times [\boldsymbol{\xi}, \boldsymbol{\xi} + d\boldsymbol{\xi}] \times [t, t + dt]$ of the phase and time spaces. It is discretized by allowing only a discrete number of equally spaced lattice points for $\boldsymbol{x}$, and a fixed number of molecular velocities $\boldsymbol{\xi}_j$. Notationally, the discretized PDF is represented by a set of functions $f_j(\boldsymbol{x}, t)$ whereby the index j means that the function refers to the discretized molecular velocity $\boldsymbol{\xi}_j$. The discretized f_j obeys the Lattice-Boltzmann equation [32]:

$$f_j(\boldsymbol{x} + \boldsymbol{\xi}_j \triangle t, t + \triangle t) - f_j(\boldsymbol{x}, t) = \triangle t \left(\Omega_j^{\mathrm{C}} + \Omega_j^{\mathrm{S}}\right). \tag{13}$$

This equation accounts for the change in the distribution function due to convection on the left-hand side, while the right-hand side incorporates the collision operator Ω_j^{C} and a

Table 1 Simulation parameters and physical constants used for simulations in the Section 5 and the part II of the current work

Parameter	Value
Dielectric constant ϵ [$\mathrm{CV}^{-1}\mathrm{m}^{-1}$]	$6.95 \cdot 10^{-10}$ [25]
Faraday constant F [$\mathrm{C\,mol}^{-1}$]	96485.33
Boltzmann constant k_B [$\mathrm{V\,CK}^{-1}$]	$1.38065 \cdot 10^{-23}$
Elementary charge e [C]	$1.602177 \cdot 10^{-19}$
Surface potential ψ_0 [V]	-0.01
Inlet velocity u_i [ms^{-1}]	0.2
Fluid viscosity ν [$\mathrm{m}^2\mathrm{s}^{-1}$]	10^{-6} [25]
Water mean free path λ_{H2O} [m]	$1.26 \cdot 10^{-10}$ [26]
Avogadro number N_A [mol^{-1}]	$6.02 \cdot 10^{23}$
Hydrogen ion diffusion constant D_{H^+} [$\mathrm{m}^2\mathrm{s}^{-1}$]	$9.31 \cdot 10^{-9}$ [27]
Phosphate ion diffusion constant $D_{\mathrm{PO}_4^{3-}}$ [$\mathrm{m}^2\mathrm{s}^{-1}$]	$0.612 \cdot 10^{-9}$ [27]
Calcium ion diffusion constant $D_{\mathrm{Ca}^{2+}}$ [$\mathrm{m}^2\mathrm{s}^{-1}$]	$0.792 \cdot 10^{-9}$ [27]
OCP saturation constant $K_{\mathrm{sp,OCP}}$ [$(\mathrm{mol\,m}^{-3})^{16}$]	$10^{-48.86}$ [28]
OCP Temkin coefficient $\sigma_{T,\mathrm{OCP}}$	1 [20]
CSH dissolution rate coefficient k_{CSH} [$\mathrm{mol\,m}^{-2}\ \mathrm{s}^{-1}$]	$3.1 \cdot 10^{-11}$ [20]
CSH saturation constant $K_{\mathrm{sp,CSH}}$ [$(\mathrm{mol\,m}^{-3})^x$]	$10^{11.15}$ [20]
CSH Temkin coefficient $\sigma_{T,\mathrm{CSH}}$	16 [29]
Phosphor acid concentration $C_{\mathrm{H_3PO_4}}$ [$\mathrm{mol\,m}^{-3}$]	0.1
Temperature T [K]	298.15
Debye-Hückel coefficent A [$\sqrt{(\mathrm{m^3mol^{-1}})}$]	0.016102
Debye-Hückel coefficent B [$\sqrt{(\mathrm{m^3m^{-2}mol^{-1}})}$]	$1.0391 \cdot 10^{8}$
Molecular distance Ca-w [m]	$2.33 \cdot 10^{-10}$ [30]
Knudsen number Kn	0.09
Discretization parameters	
Cell size $\triangle x$ [m]	$1.40045 \cdot 10^{-9}$
Time step Poisson lattice $\triangle t_{\mathrm{PE}}$ [s]	$2.45159 \cdot 10^{-19}$
Time step momentum lattice $\triangle t_{\mathrm{NSE}}$ [s]	$2.61503 \cdot 10^{-13}$
Time step ions lattice $\triangle t_{\mathrm{NPE}}$ [s]	$4.80703 \cdot 10^{-11}$

sourcing term Ω_j^S. The motion of molecules is defined by a set of discrete directions j (Fig. 3) and corresponding normalized lattice velocities $\boldsymbol{\xi}_j$ (Table 5).

For all system equations, the Bhatnagar-Gross-Krook (BGK) collision operator is employed [33]:

$$\Omega_j^{\mathrm{BGK}} = \frac{f_j^{\mathrm{eq}}(\boldsymbol{x},t) - f_j(\boldsymbol{x},t)}{\tau}, \tag{14}$$

where $f_j^{\mathrm{eq}}(\boldsymbol{x},t)$ is an approximation of the equilibrium distribution function based on the Maxwell-Boltzmann equation and discretized with Gauss-Hermite quadrature. In the

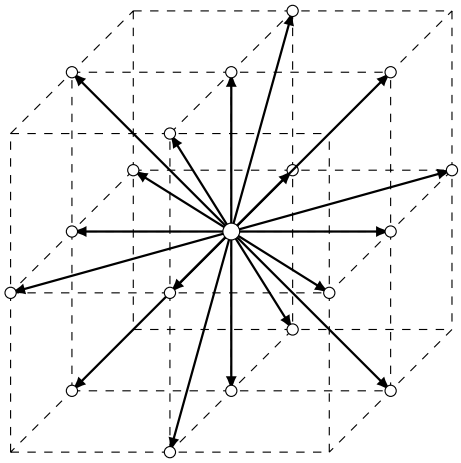

Fig. 3 Schematic view of the $D3Q19$ discrete velocity set. The discrete velocities are depicted as arrows

standard case, a second-order equilibrium distribution in LBM is written as $f_j^{\mathrm{eq}} = w_j \rho\left(1 + \frac{\boldsymbol{\xi_j}\cdot\boldsymbol{u}}{c_\mathrm{s}^2} + \frac{(\boldsymbol{\xi_j}\boldsymbol{\xi_j} - \delta_{\alpha\beta}c_\mathrm{s}^2):\boldsymbol{uu}}{2c_\mathrm{s}^4}\right)$. In general, when approximating partial differential equations (PDE) systems with the LBM, the relaxation time τ defines the rate of the PDFs' adjustment towards the equilibrium distribution. The BGK collision operator adds only a small amount of numerical diffusion [34] and remains stable in the current operating conditions due to the low velocities that occur and the relatively high relaxation times chosen.

The equilibrium functions and the source terms according to Guo et al. [35] for different equations are shown in Table 2.

The w_j are the integration weighting coefficients (Table 5), $c_\mathrm{s} = \sqrt{1/3}$ is the discrete speed of sound and $S_{\mathrm{PE/RNPE}}$ the source, which is the reaction rate in RNPE and the right equation side in PE.

In PE there is no diffusion coefficient and time derivative of potential, which is why in the case of LBM discretization the diffusion coefficient is set to one and the apparent time derivative is eliminated by reaching the converged state.

The macro-variables are recovered through the moments of PDFs (Table 3).

Pressure is included using the second order moment, but can be computed with the zeroth one [32]:

$$p = \rho c_\mathrm{s}^2. \tag{15}$$

The diffusion and viscosity coefficients in the mentioned macroscopic equations are connected to the lattice relaxation times in the LBEs in the way shown in Table 4.

The lattice stencil utilized is $D3Q19$, meaning three spatial dimensions and 19 discrete microscopic velocities, inclusive of the zero (Fig. 3 and Table 5). This choice allows

Table 2 Used LBM collision and source terms

Equation	$f_j^{\mathrm{eq}}(\boldsymbol{x},t)$	$\Omega_j^S(\boldsymbol{x},t)$
PE	$w_j\psi$	$\left(1-\frac{\triangle t}{2\tau}\right)w_j S_{\mathrm{PE}}$
RNPE	$w_j C_i\left(1+\frac{\boldsymbol{\xi_j}\cdot(\boldsymbol{u}_{\mathrm{fl}}+\boldsymbol{u}_{\mathrm{el}})}{c_{\mathrm{s}}^2}\right)$	$\left(1-\frac{\triangle t}{2\tau}\right)w_j S_{\mathrm{RNPE}}$
NSE	$w_j\rho\left(1+\frac{\boldsymbol{\xi_j}\cdot\boldsymbol{u}}{c_{\mathrm{s}}^2}+\frac{(\boldsymbol{\xi}_j\boldsymbol{\xi}_j-\delta_{\alpha\beta}c_{\mathrm{s}}^2):\boldsymbol{u}\boldsymbol{u}}{2c_{\mathrm{s}}^4}\right)$	$\left(1-\frac{\triangle t}{2\tau}\right)w_j\left(\frac{\boldsymbol{\xi_j}}{c_{\mathrm{s}}^2}+\frac{(\boldsymbol{\xi}_j\boldsymbol{\xi}_j-\delta_{\alpha\beta}c_{\mathrm{s}}^2)\cdot\boldsymbol{u}}{c_{\mathrm{s}}^4}\right)\cdot\boldsymbol{F}$

Table 3 Lattice Boltzmann PDFs moments

Equation	0th order	1st order
PE	$\psi=\sum_j f_{j,\mathrm{PE}}+\frac{1}{2}S_{\mathrm{PE}}$	$\nabla\psi=-\frac{1}{\tau_{\mathrm{PE}}c_{\mathrm{s}}^2\triangle x}\sum_j\boldsymbol{\xi_j}f_{j,\mathrm{PE}}$
RNPE	$C_i=\sum_j f_{j,\mathrm{RNPE}}+\frac{1}{2}S_{\mathrm{RNPE}}$	–
NSE	$\rho=\sum_j f_{j,\mathrm{NSE}}$	$\boldsymbol{u}=\sum_j\boldsymbol{\xi_j}f_{j,\mathrm{NSE}}+\frac{1}{2}\boldsymbol{F}$

Table 4 Diffusion parameters conversion to relaxation times for equations used in the current simulation model

Equation	Diffusion parameter in LBM
PE	$D=\left(\tau_{\mathrm{PE}}-\frac{1}{2}\right)c_{\mathrm{s}}^2\frac{\triangle x^2}{\triangle t}=1$
RNPE	$D_i=\left(\tau_{\mathrm{RNPE}}-\frac{1}{2}\right)c_{\mathrm{s}}^2\frac{\triangle x^2}{\triangle t}$
NSE	$\nu=\left(\tau_{\mathrm{NSE}}-\frac{1}{2}\right)c_{\mathrm{s}}^2\frac{\triangle x^2}{\triangle t}$

Table 5 Lattice discretization parameters

Directions j	Normalized lattice velocity $\boldsymbol{\xi}_j$	Lattice weights w_j
0	(0, 0)	1/3
$1,2,\ldots,6$	$(\pm1,0,0),(0,\pm1,0),(0,0,\pm1)$	1/18
$7,8,\ldots,18$	$(\pm1,\pm1,0),(\pm1,0,\pm1),(0,\pm1,\pm1)$	1/36

us to minimize memory and computational power requirements while achieving a sufficiently high accuracy when calculating potential gradients.

Classical LBM deals with nondimensionalized quantities in so-called lattice units, which are in our case calculated in a way, so that $\triangle x=\triangle t=1$ in lattice units. The physical values of cell size and time step size are used as conversion factors and can be found in Table 1. The other conversion factors are combinations of these two and the density conversion factor, which is in our case water density 1000 kgm^{-3}. The NSE approximation with LBM is performed in the classical way using the described units conversion method. For the PE and NPE, conversion is realized only partially. The transport (advection–diffusion) equation (ADE) can be used for arbitrary dimensionalized or nondimensionalized scalars, which is why we let the concentrations and electric potential have SI dimensions. The only term which needs special conversion is the source term, because it describes the change of the dimensionalized or nondimensionalized quantity in time, which is in lattice units. So, we multiply the source term of each ADE with the time conversion factor.

3.2 Boundary conditions in LBM

3.2.1 NSE boundary conditions

In LBM, boundary conditions are usually applied to the PDFs rather than to the macroscopic variables, which makes the entire procedure more complex. For Dirichlet-type boundary conditions from the LBM point of view, the wet-node non-equilibrium approach is used [36]. Thereby, populations at the boundary lattice points $(\boldsymbol{x}_p)$ are constructed from both equilibrium f_j^{eq} and non-equilibrium populations f_j^{neq}. If the velocity is fixed and the pressure is treated with the Neumann boundary condition, the following scheme is applied: in the equilibrium part, the velocity is prescribed from the macro-level and density ρ_{rec} is reconstructed from incoming populations. The non-equilibrium part is computed from stress tensor components received through finite differences in neighbor fluid cells $S_{\alpha\beta}^{\mathrm{FD}}$:

$$f_{j,\mathrm{NSE}}(\boldsymbol{x}_p)=f_{j,\mathrm{NSE}}^{\mathrm{eq}}(\rho_{\mathrm{rec}},u_n(\boldsymbol{x}_p))+f_{j,NSE}^{\mathrm{neq}}(S_{\alpha\beta}^{\mathrm{FD}}), \tag{16}$$

$$\rho_{\mathrm{rec}}=\frac{1}{1-\boldsymbol{n}\cdot\boldsymbol{u}}\left(\rho_0+2\rho_+\right), \tag{17}$$

$$\rho_0=\sum_{j}^{\text{along boundary}} f_{j,\mathrm{NSE}}, \tag{18}$$

$$\rho_+ = \sum_{j}^{\text{towards boundary}} f_{j,\text{NSE}}, \tag{19}$$

$$f^{\text{neq}}_{j,\text{NSE}}(S^{\text{FD}}_{\alpha\beta}) = w_j \frac{(\xi_{j,\alpha}\xi_{j,\beta} - c_s^2\delta_{\alpha\beta})}{2c_s^4} S^{\text{FD}}_{\alpha\beta}. \tag{20}$$

At the walls, no-slip boundary condition can be applied, which is realized through the full-way bounce-back of incoming populations at the wall [37]:

$$f_{\bar{j}}(\boldsymbol{x}_p, t + \triangle t) = f_{j,\text{pre-stream}}(\boldsymbol{x}_p, t), \tag{21}$$

$$\boldsymbol{\xi}_{\bar{j}} = -\boldsymbol{\xi}_j. \tag{22}$$

In our case, by microfluidics, free-slip boundary condition is assumed, which is similar to bounce-back but considers the local wall normal. The specular reflection is applied, where, depending on the discrete normal, the populations are reflected in the mirrored direction [38].

The zero-gradient boundary condition in LBM is realized by copying the averaged PDF along the lattice direction:

$$f_{j,\text{post-stream}}(\boldsymbol{x}_p) = f_{j,\text{post-stream}}(\boldsymbol{x}_p - \boldsymbol{\xi}_j \triangle t). \tag{23}$$

3.2.2 ADE boundary conditions

At the mesoscopic level by ADE, the velocity is always known from the precomputed NSE. So, by the Dirichlet boundary condition, the transported scalar is fixed and is thus put in the PDFs with a moment-based approach [39]:

$$f_{j,\text{ADE,unknown}}(\boldsymbol{x}_p) = s(\boldsymbol{x}_p) - \sum_{j,\text{known}} f_{j,\text{ADE}}. \tag{24}$$

Known populations are here those that come from neighboring fluid cells. The unknown is the population that comes from the wall. By the Neumann boundary condition, an average value of two neighboring cell populations in the current lattice direction is taken:

$$f_{j,\text{ADE}}(\boldsymbol{x}_p) = \frac{1}{2}(f_{j,\text{ADE}}(\boldsymbol{x} - \boldsymbol{\xi_j} \cdot \boldsymbol{n}) + f_{j,\text{ADE}}(\boldsymbol{x} - 2\boldsymbol{\xi_j} \cdot \boldsymbol{n})). \tag{25}$$

At the walls, bounce-back is applied as the zero-gradient boundary condition.

More information on methods for boundary conditions in LBM is provided in [32] and references therein.

3.3 Automatic differentiation (AD) with operator overloading

The goal of the current work is to determine the influence of the model parameters, and to understand which particle and which process settings lead to the highest crystallization potential—highest saturation product. Several approaches are available for the numerical computation of the *sensitivities* $\frac{dJ}{db_d}$, $d = 1, \ldots, D$, of a quantity J with respect to design variables $b_1, ..., b_d$ (in this context called control variables). Here, we briefly recapitulate them. For a concise introduction, we refer to [40].

- The simplest method is the computation of *forward difference quotients*, where the derivative $\frac{dJ}{db_d}$ is approximated as

$$\frac{dJ}{db_d} \approx \frac{J(b + \mu|b_d|v_d) - J(b)}{\mu} \tag{26}$$

for $d = 1, \ldots, D$, respectively. Here, v_d denotes the dth unit vector and μ is the stencil step width. The optimal choice for the step width is $\mu \approx \eta^{1/2}$, where η is the machine precision, balancing truncation and cancellation errors. The scheme results is executing the primal simulation D times.

- Computation of *central difference quotients* is a more accurate, but also more expensive variant of the one described above. Here, we use the approximation

$$\frac{dJ}{db_d} \approx \frac{J(b + \mu|b_d|v_d) - J(b - \mu|b_d|v_d)}{2\mu} \tag{27}$$

for $d = 1, \ldots, D$ with $\mu \approx \eta^{1/3}$, which results in executing $2D$ times the primal simulation.

- *Forward automatic differentiation* (AD) treats each variable X as a vector $\left[X, \frac{\partial X}{\partial b_1}, ..., \frac{\partial X}{\partial b_d}\right] \in \mathbb{R}^{D+1}$, which contains the value as well as the sensitivities with respect to the control variables. For initialization, the sensitivity of a control parameter b_d with respect to another

control $b_{d'}$, $d, d' = 1, \ldots, D$, is $\delta_{d,d'}$. The derivative components are then processed according to the derivation combination rules during all mathematical operations. E.g., the product Z of two variables X, Y is

$$\left[Z, \frac{\partial Z}{\partial b_1}, ..., \frac{\partial Z}{\partial b_d}\right] := \left[XY, X\frac{\partial Y}{\partial b_1} + Y\frac{\partial X}{\partial b_1}, ..., X\frac{\partial Y}{\partial b_d} + Y\frac{\partial X}{\partial b_d}\right].$$

The whole program is executed similar to the standard program. At the end, one arrives to the quantity of interest J and its sensitivities $\frac{dJ}{db_d}$, $d = 1, \ldots, D$. The computational costs grow proportionally to D and, in contrast to finite difference methods, optimal accuracy at machine precision is observed. Similarly to the above methods, this method is generic and well-suited for time-dependent problems, coupled problems and nonstandard boundary conditions. For both numerical and computational performance evaluation of AD in the context of (LBM) fluid flow problems, we refer to [41–44].

- *Adjoint methods* solve the adjoint PDE system in order to compute the sensitivities $\frac{dJ}{db_d}$ from the adjoint solution. Unlike the above approaches, solving one adjoint system allows to compute arbitrarily many sensitivities. Hence, the computational effort is independent from D. The approach is less generic, e.g., for different boundary conditions, a new adjoint system needs to be deduced. Moreover, since the adjoint system evolves backwards in time, complex and costly checkpointing methods have to be employed in order to treat time-dependent problems.
- *Reverse automatic differentiation* can be interpreted as an automatic variant to the operation of deriving an adjoint system and solving it for the sensitivites. It is fully generic, but inherits the problems that adjoint methods have with time-dependent problems.

Keeping in mind the requirements of time dependence and accuracy (Sect. 5.3), we employ forward AD in this work. To do so, it needs to be guaranteed that each single mathematical operation used in the program is differentiable (at least in a subdifferential sense). In *OpenLB*, forward AD is then implemented via C++ operator overloading by a data type ADf<T,D> which stores for any quantity X its value as well as its n sensitivities with respect to the controls. For example, the overloading multiplication operator for variables of type ADf<double,n> looks like

```
// template with precision T and number of derivatives D as arguments
template <class T, unsigned D>
inline constexpr ADf<T,D>& ADf<T,D>::operator *= (const ADf<T,D>& Y) {
  // _v stores the value, _d stores the derivative vector
  // multiplication rule by calculating derivative
  _d = _d*Y._v+_v*Y._d;
  _v *= Y._v;
  return *this;
}
```

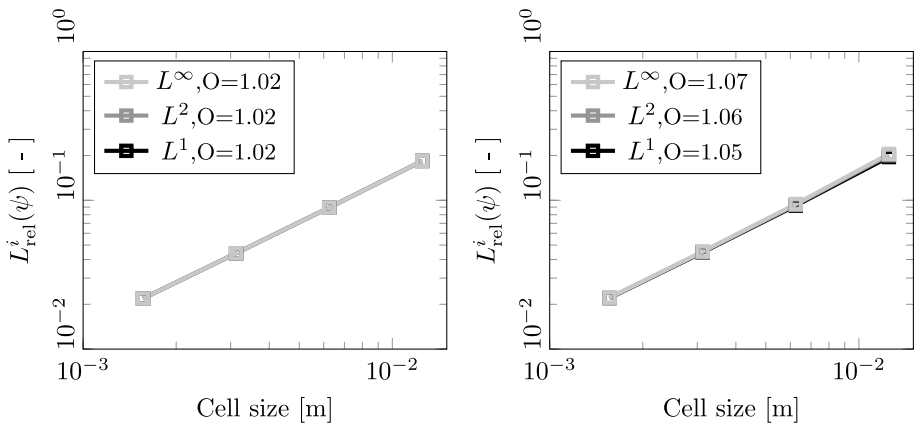

(a) $\tau = 1$ (b) $\tau = 0.6$

Fig. 4 Convergence plot of the discretized Poisson equation by two different relaxation times. Evaluation criterion is the relative error norms of the electric potential by comparison with analytical solution [45]

Therefore, the data type used for floating-point variables in the entire code basis is employed as a template parameter. This allows compilation run of the same function with both IEEE `double` precision (for primal simulation) and ADf<double,D> (for derivative computation) type variables. The result is a generic method, which reuses the same setup for both the primal simulation and the sensitivity analysis.

3.4 Simulation algorithm for RNSPNPE on example of OCP supersaturation with coupled AD

Below, the simulation algorithm with AD with respect to a variable α performed at each lattice point is presented.

4 Step-wise validation and analysis of the electric hydrodynamic LBM model

Due to the complexity of the described model, its parts are validated separately against analytical solutions. All the test cases are one-dimensional, but they are solved on three-dimensional lattices with periodic boundaries in the other directions. All the examples are computed until convergence of the spatially averaged electric potential is achieved based on the following criterion:

$$\frac{\frac{1}{N_t}\sum_l^{N_t}(\psi_{\mathrm{avg},l}-\sum_m^{N_t}\psi_{\mathrm{avg},m})^2}{\sum_m^{N_t}\psi_{\mathrm{avg},m}} < 10^{-9} \tag{28}$$

// Initialization
if boundary cell **then**
    Apply ADE boundary conditions with initial values for PE
    for each solved ion **do**
        Apply ADE boundary conditions with initial values for RNPE
    end for
    Apply boundary conditions with initial values for NSE
end if
Initialize f_j^{eq} with given initial values
// Main simulation loop
for each $t \leq t_{\max}$ **do**
    // LB simulation steps
    while $\frac{\frac{1}{N_t}\sum_l^{N_t}(\psi_{\mathrm{avg},l}-\sum_m^{N_t}\psi_{\mathrm{avg},m})^2}{\sum_m^{N_t}\psi_{\mathrm{avg},m}} > \varepsilon$ **do** *// Poisson loop*
        Collision and streaming for PE of a vector $(f_{j,\mathbf{PE}}, \partial_\alpha f_{j,\mathbf{PE}})$ ▷ Eq. (4)
    end while
    for each solved ion **do**
        if boundary cell **then**
            Apply ADE boundary conditions for RNPE
        end if
        Collision and streaming for RNPE of a vector $(f_{j,i,\mathbf{RNPE}}, \partial_\alpha f_{j,i,\mathbf{RNPE}})$ ▷ Eq. (1)
    end for
    if boundary cell **then**
        Apply boundary conditions for NSE
    end if
    Collision and streaming for carrier fluid NSE of a vector $(f_{j,\mathbf{NSE}}, \partial_\alpha f_{j,\mathbf{NSE}})$ ▷ Eq. (3)
    // Post-processing
    Calculate Poisson eq. source term $S_{\mathbf{PE}}$ and $\partial_\alpha S_{\mathbf{PE}}$ ▷ Eq. (4)
    for each solved ion **do**
        Calculate $\boldsymbol{u}_{\mathrm{el}}$ for each solved ion and their derivatives w.r.t. α ▷ Eq. (5)
    end for
    Calculate $\boldsymbol{F}_{\mathrm{el}}$ for the carrier fluid and its derivative w.r.t α ▷ Eq. (6)
    for each boundary cell **do**
        Calculate r_{diss}, $\partial_\alpha r_{\mathrm{diss}}$ ▷ Eq. (9)
        Calculate $\Omega_{\mathrm{OCP}} = \left(\frac{\mathrm{IAP}_{\mathrm{OCP}}}{K_{\mathrm{sp,OCP}}}\right)^{\frac{1}{\sigma_{\mathrm{T,OCP}}}}$ and $\partial_\alpha \Omega_{\mathrm{OCP}}$
    end for
end for

where N_t is the number of time steps at which the convergence of PE was checked. All the cases are steady-state without time dependence, so that there is no need for an internal PE simulation loop. All the discretized equations are calculated once per time step.

4.1 Poisson equation

The PE for validation test, which is taken from [45], is defined as

$$\Delta\psi = h^2\psi, \tag{29}$$

with according boundaries

$$\psi_{x=0} = \psi_{x=1} = 1, \tag{30}$$

$$h = 27.79 \tag{31}$$

and analytical solution

$$\psi(x) = \frac{e^h - 1}{e^h - e^{-h}} e^{-hx} + \frac{1 - e^{-h}}{e^h - e^{-h}} e^{hx} \tag{32}$$

The convergence behavior of the discretized PE is shown in Fig. 4. Three different relative error norms (L^1, L^2, L^∞) between the analytical ψ_a and numerical solutions ψ_n of the Eq. 29 are shown.

$$L^1_{\text{rel}}(\psi) = \frac{\sum_{c=1}^{N_{\text{node}}} |\psi_a - \psi_n|}{\sum_{c=1}^{N_{\text{node}}} |\psi_a|}, \tag{33}$$

$$L^2_{\text{rel}}(\psi) = \sqrt{\frac{\sum_{c=1}^{N_{\text{node}}} |\psi_a - \psi_n|^2}{\sum_{c=1}^{N_{\text{node}}} |\psi_a|^2}}, \tag{34}$$

$$L^\infty_{\text{rel}}(\psi) = \frac{\max\limits_{c=1,..,N_{\text{node}}} |\psi_a - \psi_n|}{\max\limits_{c=1,..,N_{\text{node}}} |\psi_a|}, \tag{35}$$

It can be seen that the lines have a slope of approximately one, independent of the chosen relaxation time τ. According to these results, the simulation ansatz is considered to be convergent.

4.2 Poisson-Nernst-Planck equation system

The ideal case for the PNPE system is the analytically-solvable Poisson-Boltzmann equation, which describes the Gouy-Chapman model for ionic solutions close to a charged surface [11]. The PNPE system can be written for monovalent cations and anions as:

$$\Delta\psi + \frac{F}{\epsilon}(C_+ - C_-) = 0, \tag{36}$$

$$\partial_t C_+ - \left(\frac{De}{k_B T}\nabla\psi\right)\nabla C_+ = D\Delta C_+, \tag{37}$$

$$\partial_t C_- + \left(\frac{De}{k_B T}\nabla\psi\right)\nabla C_- = D\Delta C_-, \tag{38}$$

whereas the boundary conditions are described as:

$$\psi_{x=0} = -0.02V \quad \psi_{x=L} = 0V, \tag{39}$$

$$\nabla C_{\pm,x=0} = 0 \text{ (bounce-back)} \quad C_{\pm,x=L} = 0.01\text{mol m}^{-3} \tag{40}$$

The diffusion constant D is set to 10^{-8} m^2 s^{-1}, temperature T to 298 K, dielectric constant ϵ to $6.95 \cdot 10^{-10}$ CV^{-1} m^{-1}. The Faraday constant F is $9.649 \cdot 10^4$ C mol^{-1}4, the elementary charge e equals $1.602 \cdot 10^{-19}$ C. The computation domain length L is set to 13 Debye lengths λ_D, which is

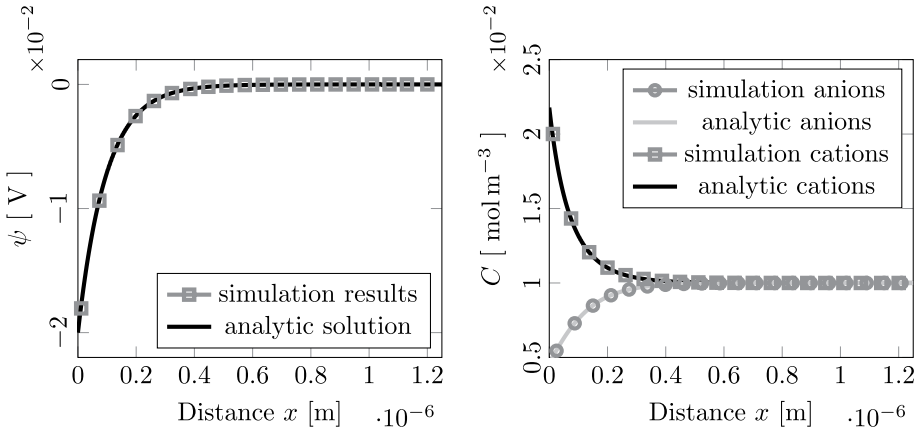

(a) Potential along the axis

(b) Concentrations along the axis

Fig. 5 Comparison of the electric potential and concentration profiles computed with discretized PNPE system and derived from the Poisson-Boltzmann equation [11]

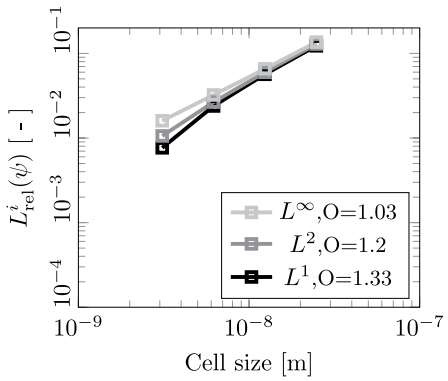

(a) Potential ψ convergence

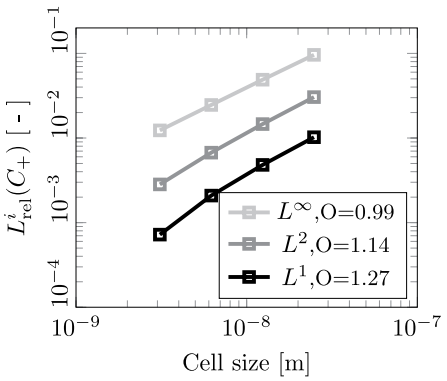

(b) Cation concentration C_+ convergence

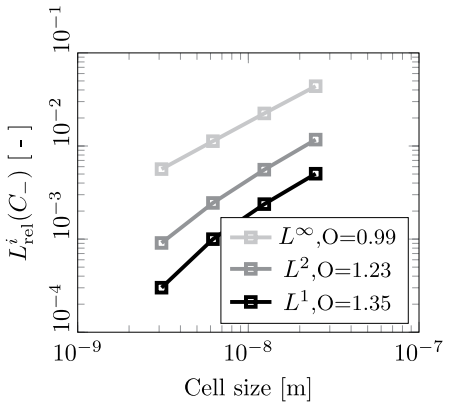

(c) Anion concentration C_- convergence

Fig. 6 Convergence plot of the PNPE system based on the analytical solution of the Poisson-Boltzmann equation for the Gouy-Chapman model [11]

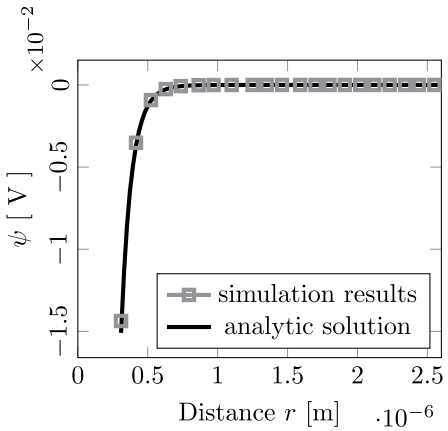

(a) Potential along the box diagonal

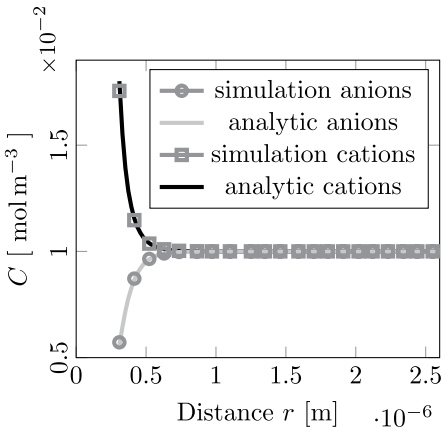

(b) Concentrations along the box diagonal

Fig. 7 Comparison of the electric potential and concentration profiles computed with discretized PNPE system and derived from the Poisson-Boltzmann equation for the 3D case with a sphere

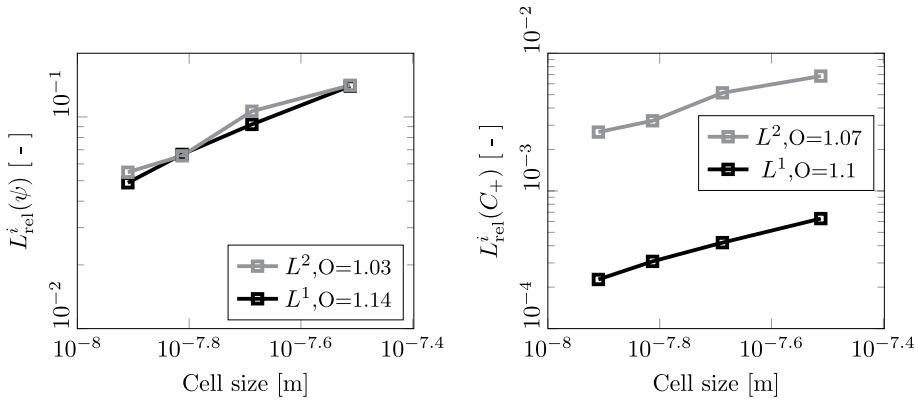

(a) Potential ψ convergence

(b) Cation concentration C_+ convergence

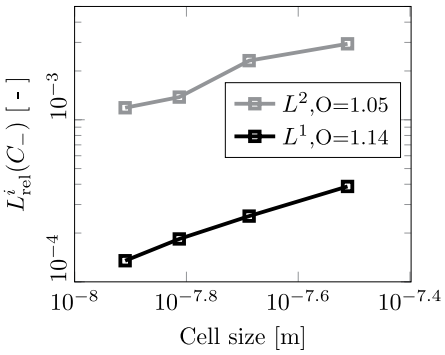

(c) Anion concentration C_- convergence

Fig. 8 Convergence plot of the PNPE system based on the analytical solution of the Poisson-Boltzmann equation for the Gouy-Chapman model for a 3D sphere test

$$\lambda_{\mathrm{D}} = \sqrt{\frac{\epsilon k_{\mathrm{B}} T}{2e^2 C_{x=L} N_A}}. \tag{41}$$

This characteristic length represents the distance at which the electric potential ψ falls by $\frac{1}{e}$. The Avogadro number N_A is defined as $6.02 \cdot 10^{23}$ 1/mol. The λ_{D} and L for this simulation are 2.98 and 35.8 µm respectively.

The analytical solution for this setup is the solution for the Poisson-Boltzmann equation [11]:

$$\psi(x) = \psi_{x=0} \exp\left(-\frac{x}{\lambda_{\mathrm{D}}}\right), \tag{42}$$

$$C_{\pm}(x) = C_{\pm,x=L} \exp\left(\mp \frac{e\psi(x)}{k_{\mathrm{B}} T}\right) \tag{43}$$

A comparison of the analytical solutions above with the simulation results is shown in Fig. 5.

This plot shows an agreement of simulated and analytical solutions of both counter-ions concentrations and the potential along the surface normal. The convergence orders of error norms can be found in Fig. 6, demonstrating approximately first order convergence of the system.

4.2.1 Three-dimensional PNPE test

Now, we construct a three-dimensional test with an analytical solution for the given PNPE system. For that, a sphere with a radius of $3\lambda_D$ is placed into a center (0, 0, 0) of a box with a side length of $32\lambda_D$. The boundary conditions are similar to the previous case:

$$\psi_{r=R_{\text{sphere}}} = -0.02V \quad \psi_{r=\infty} = 0V, \tag{44}$$

$$\nabla C_{\pm,r=R_{\text{sphere}}} = 0 \text{ (bounce-back)} \quad C_{\pm,r=\infty} = 0.01\text{mol}\,\text{m}^{-3}. \tag{45}$$

The analytical solution for the Poisson-Boltzmann equation looks a bit different [46]:

$$\psi(x) = \psi_{r=R_{\text{sphere}}} \frac{R_{\text{sphere}}}{r} \exp\left(-\frac{r - R_{\text{sphere}}}{\lambda_{\mathrm{D}}}\right), \tag{46}$$

$$C_{\pm}(r=\infty) = C_{\pm,r=\infty} \exp\left(\mp \frac{e\psi(r)}{k_{\mathrm{B}} T}\right) \tag{47}$$

A comparison of the analytical solutions above with the simulation results for this 3D case is given in Fig. 7.

This plot shows as well an agreement of simulated and analytical solutions of both counter-ions concentrations and the potential along the surface normal. The convergence

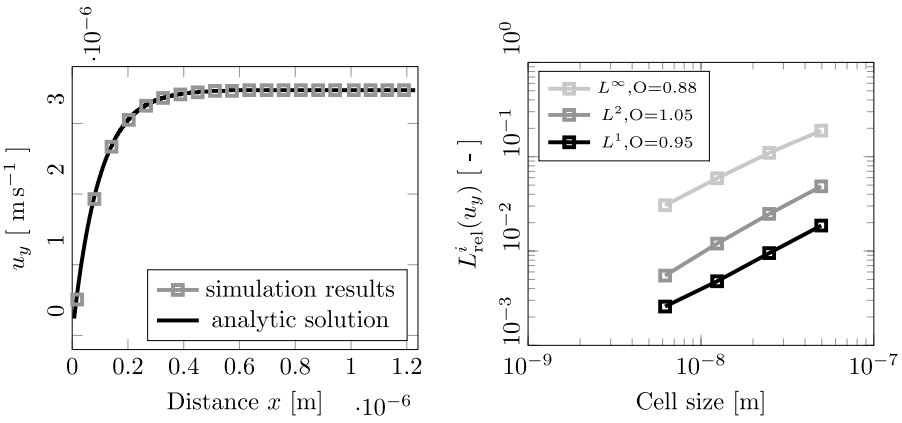

(a) **NSPNPE** velocity validation

(b) Convergence of the discretized **NSPNPE** system

Fig. 9 Validation of the NSPNPE model LBM discretization using analytical solution for electro-osmosis [25]

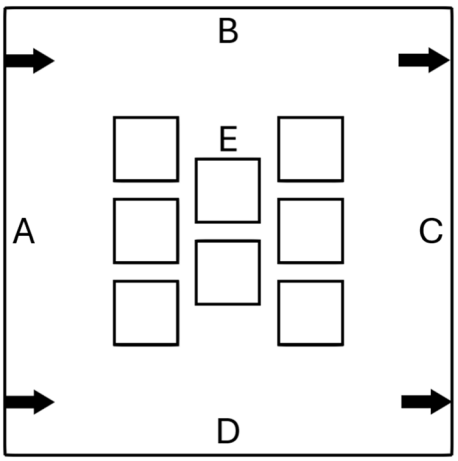

Fig. 10 Simulation domain for sensitivity algorithm evaluation. Cuboids in the center (**E**) represent porous solid particle, where calcium ions dissolve and the OCP saturation occurs in the boundary cells. **A**–**D** Are the outer domain boundaries that are considered as bulk with dissolved phosphate and hydrogen ions

orders of error norms can be found in Fig. 8, demonstrating as well approximately first-order convergence of the system.

4.3 Navier–Stokes-Poisson-Nernst-Planck equation system

The full electro-dynamic system for two monovalent counter-ions is the same as in the previous example, with the addition of equations (2) and (3). The reference solution is also the Poisson-Boltzmann equation. The electric force present in the momentum equation is much smaller than the advection term in the Nernst-Planck equations, and therefore the influence of the carrier fluid without an external electric field in the Gouy-Chapman model is assumed to be negligible. The convergence order in the system remains the same as above.

To check the convergence behavior of the complete NSPNPE system, the steady-state one-dimensional electro-osmotic flow is reproduced.

$$\Delta\psi + \frac{F}{\epsilon}(C_+ - C_-) = 0, \tag{48}$$

$$\partial_t C_+ - \Big(\frac{De}{k_{\mathrm{B}}T}\nabla\psi\Big)\nabla C_+ = D\Delta C_+, \tag{49}$$

$$\partial_t C_- + \Big(\frac{De}{k_{\mathrm{B}}T}\nabla\psi\Big)\nabla C_- = D\Delta C_-, \tag{50}$$

$$\partial_t u_y + u_x\partial_y u_y + u_y\partial_x u_y + \frac{1}{\rho}\partial_y p = \nu(\partial_x^2 u_y + \partial_y^2 u_y) + \frac{F_{\mathrm{el},y}}{\rho}. \tag{51}$$

The boundary conditions are similar to the previous case (Eqs. 44, 45). For the carrier fluid, the velocity on the wall is set to zero (bounce-back condition), whereby in the bulk boundary opposite to the wall it is set as zero-gradient. Instead of the internal electric field based on the potential gradients, a constant external field is applied in the y-direction, parallel to the wall. The only force acting within the system is also directed towards the y direction:

$$F_{\mathrm{el},y} = E_y F \sum_i z_i C_i. \tag{52}$$

In the current case, $E_y = 250\ \mathrm{V\,m^{-1}}$. The analytical solution for carrier fluid velocity in the normal-to-wall direction is [25]:

$$u_y(x) = -\frac{\epsilon\psi_{x=0}E_y}{\nu\rho}\Big(1 - \frac{e^{\frac{x}{\lambda_{\mathrm{D}}}} + e^{\frac{2L-x}{\lambda_{\mathrm{D}}}}}{1 + e^{\frac{2L}{\lambda_{\mathrm{D}}}}}\Big). \tag{53}$$

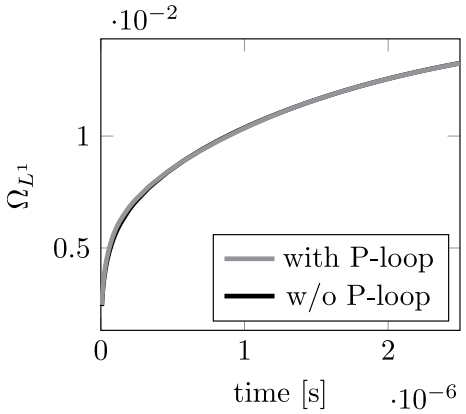

Fig. 11 Temporal development of the saturation product Ω_{OCP} with and without PE full convergence per global time step

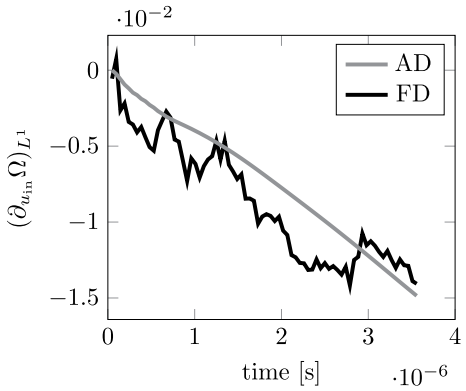

Fig. 12 Temporal development of the saturation product sensitivity with respect to the inlet velocity calculated using FD and AD

The convergence plot of the velocity error norms is shown below (Fig. 9).

The velocity shows a convergent behavior as well, and therefore the full NSPNPE system can be now held for validated. All the system components and all variables show first-order convergence, and therefore the full system is considered as a consistent model for a crystallization potential assessing electro-dynamic simulation. Such an order of convergence is caused by the boundary conditions, which reduce the second-order convergence of BGK collision, down to the first order. In future works, the boundary conditions will be enhanced in order to achieve a global second-order convergence.

5 Sensitivity assessing algorithm test

5.1 Simulation setup

We start by validating the AD sensitivity calculation on FDM results using the two-dimensional simulation domain shown in Fig. 10. The gaps between cuboids **E** are of 42.8 nm. Each cuboid has a side length of 84 nm and the distance from the outer domain boundary to the closest cuboid is 140 nm. The cell size $\triangle x$ is set to 1.4 nm. The domain boundaries **A**, **B**, **C** and **D** are treated identically. The electric potential in the fluid at the initial time step is zero. The domain boundaries **A**, **B**, **C**, and **D** are treated identically, with the electric potential set to zero. The carrier fluid is assigned a constant flow velocity of 0.2 $\mathrm{m\,s^{-1}}$ in the positive x-direction (**A**, **B**, **C**, **D**), and these outer boundaries are handled uniformly to avoid any influence from differing boundary conditions and to prevent instabilities. Hydrogen and phosphate ions are each given fixed concentrations of 0.3 and 0.1 $\mathrm{mol\,m^{-3}}$, respectively, while their concentrations inside the domain are initialized to zero to capture the diffusion of ions from the outer bulk to the pore openings and into the pores. The concentration of calcium cations, on the other hand, is set to zero at the boundaries to avoid undesirable backflow of these ions and improve boundary stability. The NPE is solved for each of the three ions.

At the Helmholtz layer next to the solid surface (boundary **E**), the electric potential is set to a constant value of -0.01 V. Its impact is investigated in the current work as well. The transported ions are reflected at the solid walls, whereby in the fluid cells touching the boundaries their concentration can be changed according to the corresponding reaction term $\sum_k R_{k,i}$. In LBM this corresponds to the bounce-back boundary condition together with a source term applied in the boundary cells. At the Knudsen number of 0.09, which is here the case, the free-slip regime for the carrier fluid velocity is considered [47]. It is a simplification of reality but this Knudsen number value belongs to the upper border of the slip regime, where we assume a slip factor striving to zero–zero-gradient velocity boundary or free-slip. The electric velocity, whose influence is much higher than the influence of the carrier fluid velocity, is still considered at the boundary cells. Knudsen diffusion and confinement effects near the wall are not considered in terms of this work. Knudsen diffusion is still much smaller than the Fickian one in the slip regime.

The list of the setup parameters and constants is shown in Table 1.

5.2 Necessity of internal Poisson equation loop

To improve simulation efficiency, only one PE step per global time step is performed instead of iterating through the entire loop. This is permissible because changes in local ion concentrations during a single global time step are minimal. The Poisson Lattice-Boltzmann equation quickly adapts to new ion configurations in response to changes in the source term, due to its short reaction time. This immediate adaptation is demonstrated in Fig. 11, which compares

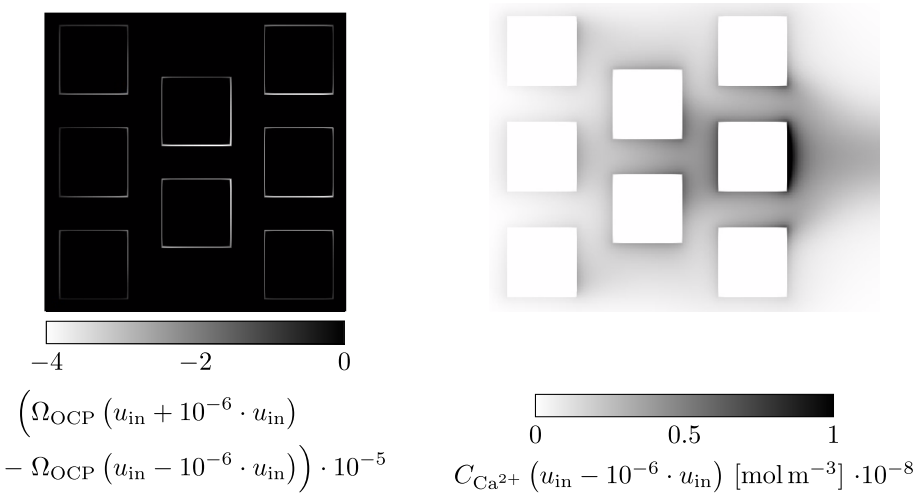

Fig. 13 Spatial distribution of the saturation products difference (left) and the calcium cation concentration (right) at the 3 μs

the averaged saturation products calculated with and without the full Poisson convergence loop.

5.3 Validation of AD with FDM applied to OCP saturation

In addition to OpenLB's extensive unit test suite [18], we assess the correctness of the AD algorithm in the current simulation setup. Figure 12 shows a comparison of the spatially averaged saturation product sensitivity to the carrier fluid inlet velocity u_{in} calculated using both the central finite difference (FD) method with a step size of 10^{-6} and the AD algorithm. The values associated to FD analysis have been computed in the following way:

$$\left(\partial_{u_{\mathrm{in}}}\Omega\right)_{L^1}(t)=\frac{\Omega_{L^1}\left(t,u_{\mathrm{in}}+10^{-6}\cdot u_{\mathrm{in}}\right)-\Omega_{L^1}\left(t,u_{\mathrm{in}}-10^{-6}\cdot u_{\mathrm{in}}\right)}{2\cdot 10^{-6}\cdot u_{\mathrm{in}}}. \tag{54}$$

Both the curves presented in Fig. 12 have similar behavior and overlapping values, and therefore, the AD algorithm can be considered as validated. These curves indicate a negative falling sensitivity of the average saturation product with respect to the inlet carrier fluid velocity. Firstly, this means that the system has not yet reached a steady state within the observed time frame. Secondly, the negative sensitivity highlights the need to reduce the inlet velocity to achieve a higher saturation product. In the case of an open-pores setup, this can be explained by the fact that higher fluid velocities cause ions to be swept away, preventing their accumulation at a single point, which is essential for maximizing the supersaturation probability.

For an optical validation of the plotted behavior of the averaged saturation product derivative, we present here the spatial distribution of the subtracted saturation products $\Omega\left(u_{\mathrm{in}}+10^{-6}\cdot u_{\mathrm{in}}\right)-\Omega\left(u_{\mathrm{in}}-10^{-6}\cdot u_{\mathrm{in}}\right)$, together with the spatial distribution of the calcium cation to ensure the presence of the reactants by the time of 3 $\mathrm{rmu}s$(Fig. 13). As we can see in the left sub-figure, the saturation products difference is negative, as plotted in Fig. 12. The right sub-figure shows how the carrier fluid velocity forces the dissolved calcium cations to leave the simulation domain in the direction of the fluid motion. More details can be found in the Part II.

6 Conclusions

In the present Part I of our two part series, a novel hydro-electrochemical simulation system for nanoporous resolved geometries is established and validated on analytical solutions. The performed tests show the possibility of omitting the internal Poisson calculation loop in the cases in which the final result is stationary or quasi-stationary, as the changes of Nernst-Planck and Navier–Stokes equations per one time step are much slower than the changes of electric potential. The coupled forward automatic differentiation algorithm used for sensitivity analysis is validated using the finite differences method. The resulting simulative investigation tool can be used for predicting different surface ionic reactions of liquids through nano-scale porous systems. In Part II of our research, this system will be applied to the phosphate crystallization reaction for the estimation of the influence factors' strength and detailed behavior analysis of distinct pore types. The investigation will be performed on simplified two-dimensional and realistic three-dimensional pore structures. Sensitivity analysis results will be discussed and tested by variation of chosen parameters in direction of calculated sensitivities.

Acknowledgements This work was performed on the HoreKa supercomputer funded by the Ministry of Science, Research and the Arts Baden-Württemberg and by the Federal Ministry of Education and Research. The current research is a part of the DFG project number 436212129 "Increase of efficiency in phosphate recovery by understanding the interaction of flow and loading processes with modeling and simulation". This work has received funding from the European Union's Horizon Europe research and innovation program under grant agreement No 101182847.

Author contributions F. Bukreev: methodology, validation, formal analysis, investigation, software, data curation, writing—original draft; A. Kummerländer: software, methodology, writing—review and editing; J. Jeßberger: methodology, software, validation, writing—review & editing; D. Teutscher: writing—review and editing; S. Ito: methodology, writing—review and editing; S. Simonis: formal analysis, data curation, writing—review and editing; Davide Dapelo: writing—review and editing; Mohaddeseh M. Nezhad: writing—review and editing; H. Nirschl: resources, funding acquisition; M.J. Krause: software, resources, funding acquisition, writing—review and editing.

Data availability No datasets were generated or analysed during the current study.

Declarations

Conflict of interest The authors declare no conflict of interest.

Generative AI and AI-assisted technologies in the writing process During the preparation of this work the authors used ChatGPT (OpenAI) in order to improve language. After using this tool, the authors reviewed and edited the content as needed and take full responsibility for the content of the publication.

References

1. Jareteg A, Maggiolo D, Sasic S, Ström H (2020) Finite-volume method for industrial-scale temperature-swing adsorption simulations. Comput Chem Eng 138:106852. https://doi.org/10.1016/j.compchemeng.2020.106852
2. Qiu H, Lv L, cai Pan B, jian Zhang Q, ming Zhang W, xing Zhang Q (2009) Critical review in adsorption kinetic models. J Zhejiang Univ-Sci A 10(5):716–724. https://doi.org/10.1631/jzus.A0820524
3. Bukreev F, Raichle F, Nirschl H, Krause MJ (2023) Simulation of adsorption processes on moving particles based on an Euler–Euler description using a lattice Boltzmann discretization. Chem Eng Sci 270:118485. https://doi.org/10.1016/j.ces.2023.118485
4. Kler PA, López EJ, Dalcín LD, Guarnieri FA, Storti MA (2009) High performance simulations of electrokinetic flow and transport in microfluidic chips. Comput Methods Appl Mech Eng 198(30):2360–2367. https://doi.org/10.1016/j.cma.2009.02.028
5. Barnett R, Municchi F, King J et al (2023) Electrochemical transport modelling and open-source simulation of pore-scale solid–liquid systems. Eng Comput 39:4129–4152. https://doi.org/10.1007/s00366-023-01828-5
6. Ryan EM, Mukherjee (2019) Mesoscale modeling in electrochemical devices—a critical perspective. Prog Energy Combust Sci 71:118–142. https://doi.org/10.1016/j.pecs.2018.11.002
7. Zhang L, Wang M (2015) Modeling of electrokinetic reactive transport in micropore using a coupled lattice Boltzmann method. J Geophys Res Solid Earth 120(5):2877–2890. https://doi.org/10.1002/2014JB011812 (https://agupubs.onlinelibrary.wiley.com/doi/pdf/10.1002/2014JB011812)
8. He X, Li N (2000) Lattice Boltzmann simulation of electrochemical systems. Comput Phys Commun 129(1):158–166. https://doi.org/10.1016/S0010-4655(00)00103-X
9. Zhang D, Liu W, Wu CY, Cai Q (2022) The development of a 3d pore-scale lattice Boltzmann model for 3d microstructure modeling and design of li-ion battery electrodes. Energ Technol 10(7):2200080. https://doi.org/10.1002/ente.202200080 (https://onlinelibrary.wiley.com/doi/pdf/10.1002/ente.202200080)
10. ICMENS '04 (2004) Proceedings of the 2004 International Conference on MEMS, NANO and Smart Systems. USA: IEEE Computer Society
11. Hunter RJ (2001) Foundations of colloid science. Oxford University Press. Available from: https://books.google.de/books?id=-UVCAQAAIAAJ
12. Ross-Jones J, Gaedtke M, Sonnick S, Rädle M, Nirschl H, Krause MJ (2019) Conjugate heat transfer through nano scale porous media to optimize vacuum insulation panels with lattice boltzmann methods. Comput Math Appl 77(1):209–221. https://doi.org/10.1016/j.camwa.2018.09.023
13. Ross-Jones J, Gaedtke M, Sonnick S, Meier M, Rädle M, Nirschl H et al (2021) Pore-scale conjugate heat transfer simulations using lattice Boltzmann methods for industrial applications. Appl Therm Eng 182:116073. https://doi.org/10.1016/j.applthermaleng.2020.116073
14. Selmi A, Bhapkar S, Nagel C, Kummerländer A, Krause MJ (2023) Simulation of temperature driven microflows using a Lattice Boltzmann method in slip and moderate transition regimes. In: 2023 24th International Conference on Thermal, Mechanical and Multi-Physics Simulation and Experiments in Microelectronics and Microsystems (EuroSimE); pp 1–6
15. Fu J, Wang M, Chen B et al (2023) A data-driven framework for permeability prediction of natural porous rocks via microstructural characterization and pore-scale simulation. Eng Comput 39:3895–3926. https://doi.org/10.1007/s00366-023-01841-8
16. Kummerländer A, Dorn M, Frank M, Krause MJ (2023) Implicit propagation of directly addressed grids in lattice Boltzmann methods. Concurrency Comput Pract Exp 35(8):e7509. https://doi.org/10.1002/cpe.7509 (https://onlinelibrary.wiley.com/doi/pdf/10.1002/cpe.7509)
17. Kummerländer A, Bukreev F, Berg S, Dorn M, Krause MJ (2024) Advances in computational process engineering using Lattice Boltzmann methods on high performance computers. In: High Performance Computing in Science and Engineering '22. Springer
18. Krause MJ, Kummerländer A, Avis SJ, Kusumaatmaja H, Dapelo D, Klemens F et al (2021) Openlb–open source lattice Boltzmann code. Comput Math Appl 81:258–288. https://doi.org/10.1016/J.CAMWA.2020.04.033
19. Kummerländer A, Avis S, Kusumaatmaja H, Bukreev F, Crocoll M, Dapelo D, et al.: OpenLB release 1.6: open ource lattice Boltzmann code. Zenodo. Available from: https://doi.org/10.5281/zenodo.7773497
20. Trapote-Barreira A, Cama J, Soler JM (2014) Dissolution kinetics of C–S–H gel: flow-through experiments. Phys Chem Earth Parts A/B/C 70-71:17–31. Mechanisms and Modelling of Waste-Cement and Cement-Host Rock Interactions. https://doi.org/10.1016/j.pce.2013.11.003
21. Graham S, Brown PW (1996) Reactions of octacalcium phosphate to form hydroxyapatite. J Cryst Growth 165(1):106–115. https://doi.org/10.1016/0022-0248(95)00994-9
22. Kim D, Mahabadi N, Jang J, van Paassen LA(2020) Assessing the kinetics and pore-scale characteristics of biological calcium carbonate precipitation in porous media using a microfluidic chip experiment. Water Resour Res 56(2):e2019WR025420.

E2019WR025420 2019WR025420. https://doi.org/10.1029/2019WR025420. https://agupubs.onlinelibrary.wiley.com/doi/pdf/10.1029/2019WR025420
23. Parkhurst DL, Appelo CAJ Description of input and examples for PHREEQC version 3–A computer program for speciation, batch-reaction, one-dimensional transport, and inverse geochemical calculations. U.S. Geological Survey. Available from: http://pubs.usgs.gov/tm/06/a43
24. Holtzer AM (1954) The collected papers of Peter J. W. Debye. Interscience, New York-London, 1954. xxi + 700 pp., \$9.50. J Polym Sci 13(72):548–548. https://doi.org/10.1002/pol.1954.120137203. https://onlinelibrary.wiley.com/doi/pdf/10.1002/pol.1954.120137203
25. Tian F, Li B, Kwok DY (2004) Lattice Boltzmann simulation of electroosmotic flows in micro- and nanochannels. In: 2004 International Conference on MEMS, NANO and Smart Systems (ICMENS'04), pp 294–299
26. Chen FF (2016) In: Diffusion and resistivity. Springer International Publishing, Cham, pp 145–185
27. Marcus Y (1997) Ion properties/Yizhak Marcus. Marcel Dekker, New York
28. Tung M, Eidelman N, Sieck B, Brown WE (1988) Octacalcium phosphate solubility product from 4 to 37-degree-c. J Res Natl Bur Stand 09(93):613. https://doi.org/10.6028/jres.093.153
29. Heughebaert J, Nancollas G (1984) Cheminform abstract: kinetics of crystallization of octacalcium phosphate. Chemischer Informationsdienst 09:15. https://doi.org/10.1002/chin.198438004
30. Marcus Y (1988) Ionic radii in aqueous solutions. Chem Rev 88(8):1475–1498. https://doi.org/10.1021/cr00090a003
31. Hänel D (2004) Molekulare Gasdynamik: Einführung in die kinetische Theorie der Gase und Lattice-Boltzmann-Methoden. Springer, Berlin
32. Krüger T, Kusumaatmaja H, Kuzmin A, Shardt O, Silva G, Viggen EM (2016) The Lattice Boltzmann method - principles and practice. Springer, Cham
33. Bhatnagar PL, Gross EP, Krook M (1954) A model for collision processes in gases. I. Small amplitude processes in charged and neutral one-component systems. Phys Rev 94:511–525. https://doi.org/10.1103/PhysRev.94.511
34. Simonis S, Frank M, Krause MJ (2020) On relaxation systems and their relation to discrete velocity Boltzmann models for scalar advection-diffusion equations. Phil Trans R Soc A 378:20190400. https://doi.org/10.1098/rsta.2019.0400
35. Guo Z, Zheng C, Shi B (2002) Discrete lattice effects on the forcing term in the lattice Boltzmann method. Phys Rev E 65:046308. https://doi.org/10.1103/PhysRevE.65.046308
36. Latt J, Chopard B, Malaspinas O, Deville M, Michler A (2008) Straight velocity boundaries in the lattice Boltzmann method. Phys Rev E 77:056703. https://doi.org/10.1103/PhysRevE.77.056703
37. He X, Luo LS (1997) Lattice Boltzmann model for the incompressible Navier-Stokes equation. J Stat Phys 88(3–4):927–944. https://doi.org/10.1023/B:JOSS.0000015179.12689.e4
38. Succi S (2002) Mesoscopic modeling of slip motion at fluid-solid interfaces with heterogeneous catalysis. Phys Rev Lett 89:064502. https://doi.org/10.1103/PhysRevLett.89.064502
39. Allen R, Reis T (2016) Moment-based boundary conditions for lattice Boltzmann simulations of natural convection in cavities. Progress Comput Fluid Dyn Int J 16(4):216–231. https://doi.org/10.1504/PCFD.2016.077296 (https://www.inderscienceonline.com/doi/pdf/10.1504/PCFD.2016.077296)
40. Griewank A, Walther A (2008) Evaluating derivatives. 2nd edn. Society for Industrial and Applied Mathematics (SIAM), Philadelphia, PA. Available from: https://doi.org/10.1137/1.9780898717761
41. Gunzburger MD (2002) Perspectives in flow control and optimization. Society for Industrial and Applied Mathematics. Available from: https://epubs.siam.org/doi/abs/10.1137/1.9780898718720
42. Krause MJ, Heuveline V (2013) Parallel fluid flow control and optimisation with lattice Boltzmann methods and automatic differentiation. Comput Fluids 07(80):28–36. https://doi.org/10.1016/j.compfluid.2012.07.026
43. Jeßberger J, Marquardt JE, Heim L, Mangold J, Bukreev F, Krause MJ (2022) Optimization of a micromixer with automatic differentiation. Fluids. https://doi.org/10.3390/fluids7050144
44. Ito S, Jeßberger J, Simonis S, Bukreev F, Kummerländer A, Zimmermann A et al (2024) Identification of reaction rate parameters from uncertain spatially distributed concentration data using gradient-based pde constrained optimization. Comput Math Appl 167:249–263. https://doi.org/10.1016/j.camwa.2024.05.026
45. Chai Z, Shi B (2008) A novel lattice Boltzmann model for the poission equation. Appl Math Model 32(10):2050–2058. https://doi.org/10.1016/j.apm.2007.06.033
46. Verwey EJW, Overbeek JTG, Nes Kv (1948) Theory of the stability of lyophobic colloids; the interaction of sol particles having an electric double layer. E. J. W. Verwey and J. Th. G. Overbeek, with the collaboration of K. van Nes. New York: Elsevier Pub. Co
47. Li Z, Li J, Yan G, Galindo-Torres S, Scheuermann A, Li L (2021) Mesoscopic model framework for liquid slip in a confined parallel-plate flow channel. Phys Rev Fluids 6:034203. https://doi.org/10.1103/PhysRevFluids.6.034203